https://doi.org/10.1038/s41586-019-1635-z

Self-coalescing flows in microfluidics for pulse-shaped delivery of reagents

Onur Gökçe[1,5], Samuel Castonguay[2], Yuksel Temiz[1], Thomas Gervais[2,3,4]* & Emmanuel Delamarche[1]*

Microfluidic systems can deliver portable point-of-care diagnostics without the need for external equipment or specialist operators, by integrating all reagents and manipulations required for a particular assay in one device[1]. A key approach is to deposit picogram quantities of dried reagents in microchannels with micrometre precision using specialized inkjet plotters[2–5]. This means that reagents can be stored for long periods of time and reconstituted spontaneously when adding a liquid sample. But it is challenging to carry out complex operations using multiple reagents, because shear flow enhances their dispersion and they tend to accumulate at moving liquid fronts, resulting in poor spatiotemporal control over the concentration profile of the reconstituted reagents[6]. One solution is to limit the rate of release of reagents into the liquid[7–10]. However, this requires the fine-tuning of different reagents, conditions and targeted operations, and cannot readily produce the complex, time-dependent multireagent concentration pulses required for sophisticated on-chip assays. Here we report and characterize a capillary flow phenomenon that we term self-coalescence, which is seen when a confined liquid with a stretched air–liquid interface is forced to 'zip' back onto itself in a microfluidic channel, thereby allowing reagent reconstitution with minimal dispersion. We provide a comprehensive framework that captures the physical underpinning of this effect. We also fabricate scalable, compact and passive microfluidic structures—'self-coalescence modules', or SCMs—that exploit and control this phenomenon in order to dissolve dried reagent deposits in aqueous solutions with precise spatiotemporal control. We show that SCMs can reconstitute multiple reagents so that they either undergo local reactions or are sequentially delivered in a flow of liquid. SCMs are easily fabricated in different materials, readily configured to enable different reagent manipulations, and readily combined with other microfluidic technologies, so should prove useful for assays, diagnostics, high-throughput screening and other technologies requiring efficient preparation and manipulation of small volumes of complex solutions.

The key to translating self-coalescence into a useful microfluidic technology is first to elicit and characterize its physical underpinnings (see also Supplementary Information, section 1), in order to demonstrate how air–liquid interfaces can be manipulated such that the characteristic time and length over which dispersion occurs scale with the width, *W*, of the microfluidic channel rather than its length, *L* (assuming that *W* is much less than *L*). To implement the concept, we use a shallow channel geometry (whose height, *H*, is much less than *W*) to confine the liquid within a Hele-Shaw cell—a quasi-two-dimensional planar flow model whereby flow is always considered to be locally parabolic and propagating in the direction of the pressure gradient[11]. Within the flow plane, the fluid is further confined laterally by a capillary pinning line (CPL)[12] that acts as a Laplace pressure barrier[13] and geometrically forces the liquid to self-coalesce—that is, to fold onto itself and release its surface free energy to spill over the CPL. Making the CPL straight creates a translational symmetry in the self-coalescence process that results in the fluid propagating at the velocity of the capillary front. In this process, following the path of least resistance, most of the flow occurs right behind the moving liquid front, where the fluid rapidly comes to a rest (Fig. 1a, b and Supplementary Video 1).

Free-boundary flows are known to be challenging to model and to compute numerically, let alone analytically[14]. A complete solution to the problem can be reached by numerical modelling. Alternatively, recognizing the conformal invariance of the advection–diffusion transport equation in shallow microfluidic devices[15], and that all boundary conditions become regular in the reference frame of the moving meniscus (Fig. 1c), a complete solution can be obtained using a Schwarz–Christoffel mapping[16] (see Supplementary Information, section 1.2). Two simple asymptotic solutions can be further derived via this conformal mapping approach to obtain the main velocity field along the CPL both near its contact point (where *x* is much less than *W*) and far downstream of the meniscus contact point (where *x* is much greater than *W*):

$$\overline{V}_{\mathrm{near}}(x,t) \approx U_m + i(U+U_m)(x+U_m t)/r \tag{1}$$

$$\overline{V}_{\mathrm{far}}(x,t) = A(W,\lambda,\theta_w)U_m \mathrm{e}^{-\frac{\pi}{W}(x+U_m t+i\lambda W)} \tag{2}$$

where the variables *x* and *t* are respectively the horizontal distance from the meniscus tip and the time elapsed; $r = \lambda W/(1+\cos\theta_{\mathrm{w}})$ is the radius of the circular meniscus; U_{m} is the meniscus velocity; *U* is the flow velocity at the inlet; $A(W, \lambda, \theta_{\mathrm{w}})$ is a constant geometric factor that depends on the channel width and wall contact angle; λ is the width fraction of the channel cross-section at which self-coalescence occurs; *i* is the imaginary unit; and e is Euler's number (Supplementary Information, section 1.5).

The exponential form of Equation (2) has been extensively studied in the case of Saffman–Taylor viscous fingering in a long straight channel, which yields a similar exponential decay of the velocity field with characteristic decay length $L_{\mathrm{d}} = W/\pi$ and time $t_{\mathrm{d}} = L_{\mathrm{d}}/U_{\mathrm{m}}$ (Fig. 1d)[17]. In the context of self-coalescence, this decay constant explains the short flow lifetime before stagnation is achieved (L_{d} is roughly 160 μm; t_{d} is approximately 240 ms; assuming that $W = 500$ μm and $U_{\mathrm{m}} = 1$ mm s^{-1}). The analytical results for these two asymptotic behaviours, as well as the full Schwarz–Christoffel mapping solution (see Supplementary Information, section 1.3), reveal a strong match with finite-element-method simulations and experiments, further verifying the model (Fig. 1e). To achieve self-coalescence the CPL can be made straight, but in general can be of any shape, from sharp turns to spirals and slow meanders. This process thus also explains the filling dynamics within capillary pumps[18] and around microfluidic phaseguides[19]—capillary structures often used to control wetting in microsystems. Even more importantly, the process reveals how the phenomena can be precisely triggered and controlled to engineer minimally dispersive flows.

---

[1]IBM Research–Zurich, Rüschlikon, Switzerland. [2]Department of Engineering Physics, École Polytechnique de Montréal (EPM), Montréal, Québec, Canada. [3]Institut du Cancer de Montréal, Montréal, Québec, Canada. [4]Centre de Recherche du Centre Hospitalier de l'Université de Montréal (CRCHUM), Montréal, Québec, Canada. [5]Present address: Institute of Neuroinformatics, University of Zurich/ETH Zurich, Zurich, Switzerland. *e-mail: thomas.gervais@polymtl.ca; emd@zurich.ibm.com

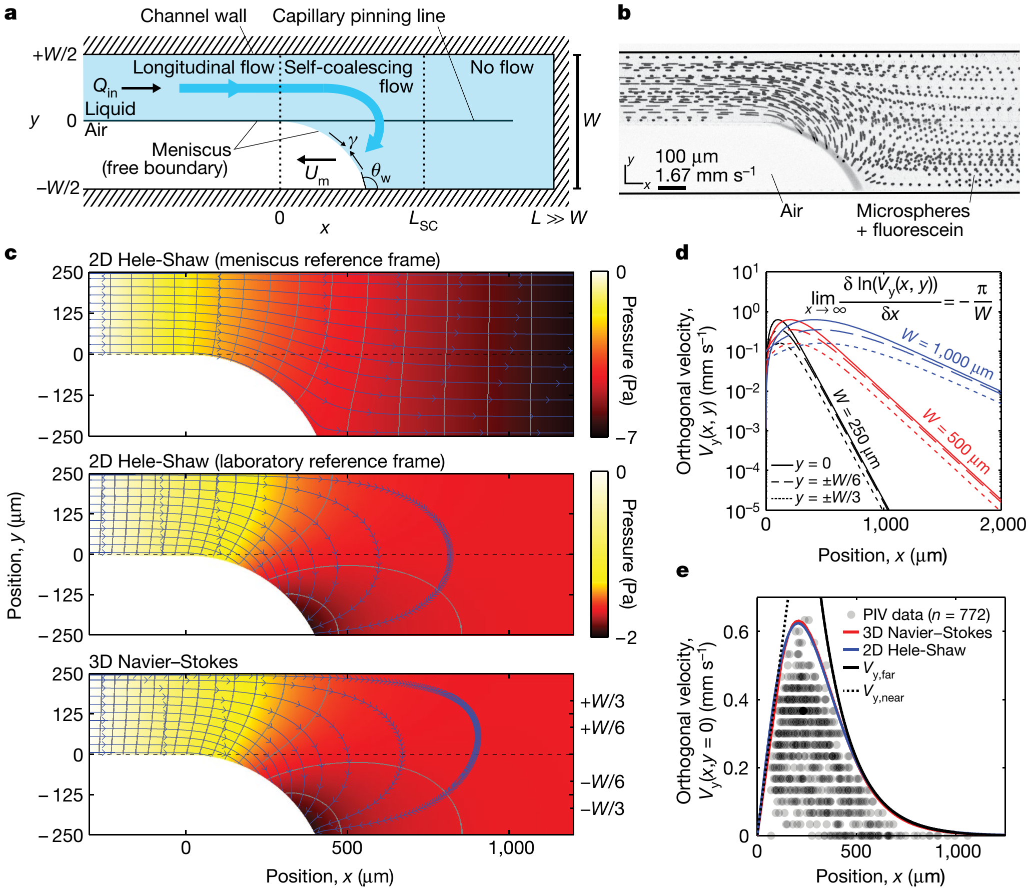

Fig. 1 | Description and modelling of self-coalescence in a microchannel. a, Top view of a microchannel (of width W and length L) that is partially filled with a liquid. During Stokes flow (at flow rate Q_{in}), this setting fosters three flow modes: longitudinal flow (where $x < 0$), self-coalescing flow ($0 < x < L_{\mathrm{SC}}$), and stagnancy ('no flow', where $x > L_{\mathrm{SC}}$), with L_{SC} being the penetration length of a self-coalescing flow. U_{m} is the meniscus velocity, γ the surface tension, and θ_{w} the contact angle. **b**, Image of fluorescent microspheres (diameter 4.8 µm) in 10 µg ml^{-1} fluorescein solution during self-coalescence (W is 500 µm; microchannel height is 50 µm; Q_{in} is 500 nl min^{-1}; Re is roughly 0.001; and $\theta_{\mathrm{w}} = 116°$). Streaks and dots respectively reveal moving and stationary particles. The CPL, implemented with a 5-µm-wide trench, is not visible after background subtraction. **c**, Two-dimensional (2D) Hele-Shaw model (top and middle) and 3D Navier–Stokes simulation (bottom) of self-coalescence in the same channel geometry as in panel **b** and at half the channel height. The colour map shows pressure, and the middle and bottom panels share the same colour map. Blue, velocity streamlines, and grey, isobars. The gaps between arrowheads show the displacement of a particle at regular time intervals (180 ms). **d**, Log plots of the orthogonal velocity (V_{y}) of self-coalescing flows for three channel widths and at different y positions as indicated, highlighting the asymptotic form of the orthogonal velocity component: near the meniscus the flow is transitional, increasing steadily until it reaches a peak and then decaying exponentially downstream of the offset. **e**, Plotted are V_{y} values for particles from all z-planes at $y = 0$ from velocimetry data (semi-transparent dots, $n = 772$ from 12 locations in 3 experiments), along with the maximum V_{y} predicted by the 2D Hele-Shaw model (blue), the 2D asymptotic model (black, $V_{\mathrm{y,far}} = 5.26\mathrm{e}^{-\pi x/500}$ mm s^{-1}; dotted, $V_{\mathrm{y,near}} = 0.0045x$ mm s^{-1}) and the 3D Navier–Stokes simulation (red). PIV, particle image velocimetry.

We use the practical implementation of self-coalescence here to control reagent reconstitution under the form of an SCM. The SCM is a microchannel having two CPLs and a vent (Fig. 2a). The first CPL (the leading barrier) ensures longitudinal flow, whereas the second (the diversion barrier) acts as a capillary burst valve[20] and prevents the liquid from exiting the SCM before the SCM is completely filled. A gap between the leading and diversion barriers forces self-coalescence to begin next to the diversion barrier. The effectiveness of reagent reconstitution using self-coalescence becomes apparent when it is compared with reconstitution in a microchannel that lacks a leading barrier, illustrated in Fig. 2b, c using amaranth dye and water. In this case, the longitudinal flow leads to the strong accumulation of amaranth dye near the liquid filling front, which creates a concentration spike that is an order of magnitude higher than the uniform concentration attained when using self-coalescence (Fig. 2d and Extended Data Fig. 1). When self-coalescence is used to reconstitute reagents printed at any fixed point in that region, the Péclet number, Pé, associated with the flows depends on the local velocity above a reagent spot, which peaks linearly (Equation (1)) before decaying exponentially with time as the meniscus moves away (Equation (2)). Thus $\mathrm{Pé} \equiv |V_{\mathrm{far}}|H/D$, which approximates to $e^{-\pi Ut/\lambda W}$, making Taylor–Aris dispersion, whose magnitude scales roughly as Pé^2, vanishingly small almost immediately after reagents have been wetted, and practically eliminating any form of convective reagent dispersion during reconstitution (Fig. 2b and Supplementary Video 2).

There are numerous ways to implement SCMs in different materials—using, for example, silicon substrates and microfabrication or polymeric materials via hot embossing or injection moulding, and using different geometries such as depressed (trench-like) or protruding (rail-like) CPLs (Extended Data Fig. 2). The material compatibility is further supported by the fact that the contact angle has only a mild influence on self-coalescence, and no influence at all on the exponential-decay length scale (Supplementary Information section 1.5). Capillary pinning can also be achieved by patterning hydrophobic layers[21].

When performing chemistry at the microscale, it is a common requirement to use solutions that have a well defined composition and volumes that range from nanolitres up to a few microlitres. The volume of the SCM determines the maximum volume of the solution

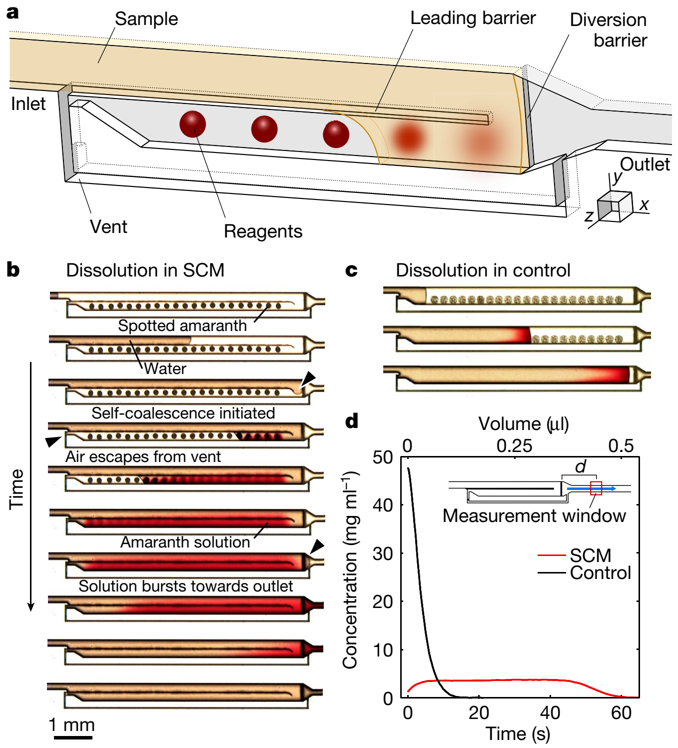

Fig. 2 | SCM for reagent reconstitution. a, Illustration of the components forming an SCM and the locations of dried, spotted reagents. **b**, Time series of bright-field microscope images showing the reconstitution of amaranth in an SCM filled with water over the course of 75 s. **c**, Reconstitution of amaranth in a control experiment (with no self-coalescence) shows strong reagent accumulation. **d**, Mean concentration profiles of amaranth solutions using a 375-nl SCM (red, $n = 6$) and a 375-nl control microchannel (black, $n = 6$, $Q_{\text{in}} = 500$ nl min^{-1}). Inset, the amaranth concentration was measured at $d = 3$ mm downstream of the SCM outlet.

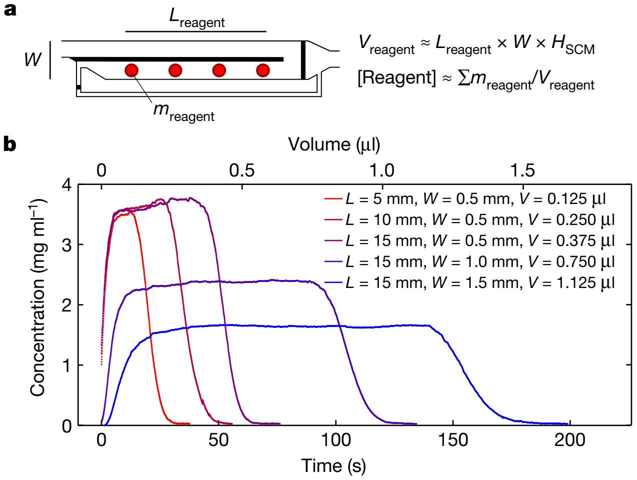

Fig. 3 | Scalability of SCMs. a, The width (W) and depth (H_{SCM}) of an SCM and the length of the deposited reagent pattern (L_{reagent}) determine the volume in which a reagent reconstitutes (V_{reagent}). The final concentration of the reagent after reconstitution can simply be adjusted with the amount of deposited reagent (m_{reagent}). **b**, Mean concentration profiles ($n = 6$; measurement distance $d = 3$ mm) of amaranth, reconstituted in SCMs with varied lateral dimensions ($H_{\text{SCM}} = 50$ μm for all; $Q_{\text{in}} = 500$ nl min^{-1}).

that can be prepared, and the amount of deposited reagent determines its resulting concentration, as demonstrated here with amaranth dye reconstitution in SCMs of different dimensions (Fig. 3 and Extended Data Fig. 3). We tested the stability of leading barriers using different channel geometries and filling conditions (Extended Data Fig. 4). Modelling and experiments reveal simple rules of thumb for designing stable SCMs: wide SCMs are preferred over long SCMs that accumulate more hydraulic resistance during filling.

The preparation of solutions with uniform concentration profiles is perhaps the greatest practical challenge solved by SCMs. In fact, any arbitrary concentration profile can be generated using one or several reagents and specific spotting patterns. However, a broadening of the initial reagent concentration profile is inevitable owing to Taylor–Aris dispersion once the solution sets in motion and exits the SCM (Supplementary Information, section 2.2). The magnitude of the dispersion and the resulting concentration profile at time t and distance d from the diversion barrier can be computed exactly by convolving the spotted reagent profile with the Green's functions that describe reagent profile evolution during SCM filling and reagent delivery (Supplementary Information, section 2.3). The approach yields a powerful design tool, which we use for reagent pulse shaping under Taylor–Aris dispersion in a way that is conceptually analogous to optical amplitude pulse shaping in dispersive media[22], where the spatial frequency distribution of the input concentration signal replaces the frequency content of a light pulse, concentration replaces the pulse amplitude, and the dispersive channel acts as the dispersive optical medium (Supplementary Information, section 2.4).

This modelling strategy for concentration pulse shaping allows us to define spotting patterns that will give specific concentration profiles of reconstituted amaranth and brilliant blue dye without having to optimize the patterns empirically (Fig. 4). We can readily release reagents consecutively with minimal intermixing (Fig. 4a), achieve steady concentration ranges (Fig. 4b), and merge reagents at preprogrammed distances downstream (Fig. 4c). It is also possible to integrate two different reagents and release them downstream either sequentially with minimum dispersion (Supplementary Information, section 2.5) and a separated profile (Fig. 4d), or mixed with an intercalated profile (Fig. 4e), or with a gradient/counter-gradient profile (Fig. 4f), in close agreement with the theoretical predictions of our concentration pulse shaping model (Extended Data Fig. 5 and Supplementary Information, section 2.6).

SCM variants that have a modified vent to purge a surplus of liquid and no diversion barrier can maintain the distribution profiles of reconstituted reagents for long durations, with minimal diffusion effects. This allows several biochemical reactions to be run in spatially segregated regions inside single SCMs, akin to using individual wells in a microtitre plate to perform simultaneous experiments (Fig. 5). We illustrate this with a multistep enzymatic assay that uses a fluorometric readout to quantify the activity of glucose-6-phosphate dehydrogenase (G6PDH)[23], with a glucose-6-phosphate (G6P) substrate, the co-factors nicotinamide adenine dinucleotide phosphate (NADP$^+$) and magnesium (Mg^{2+}), and a fluorescent reporter system that is based on the reduction of resazurin by diaphorase spotted in a first SCM (SCM 1) (Fig. 5a; note that diaphorase is spotted separately from its substrates in order to avoid undesired enzymatic activity during storage of the SCM). When the carrier fluid is introduced, these reagents reconstitute homogeneously and proceed to the next SCM, where reaction kinetics (which depend on the G6PDH concentration) can be characterized using the fluorescence signal of resorufin. SCMs are also powerful tools for calibrating such an enzymatic reaction, where the ambient temperature, slight variations in the amount of deposited reagents, or the possible decay of reagents over time might alter the reaction kinetics. Such a calibration can be performed by spotting a gradient of G6PDH in SCM 2 and measuring the resulting kinetics (Fig. 5a). The amount of deposited G6PDH and the maximum speed of the enzymatic reaction (Fig. 5b) exhibit the expected linear relation, as shown by a calibration curve (Fig. 5c, black). These calibration data match quantification data (Fig. 5c, orange), which were obtained by loading a buffer spiked with various amounts of G6PDH into SCMs containing all other reagents. It was possible to measure in only 2 min as little as 0.75 μU μl^{-1} of

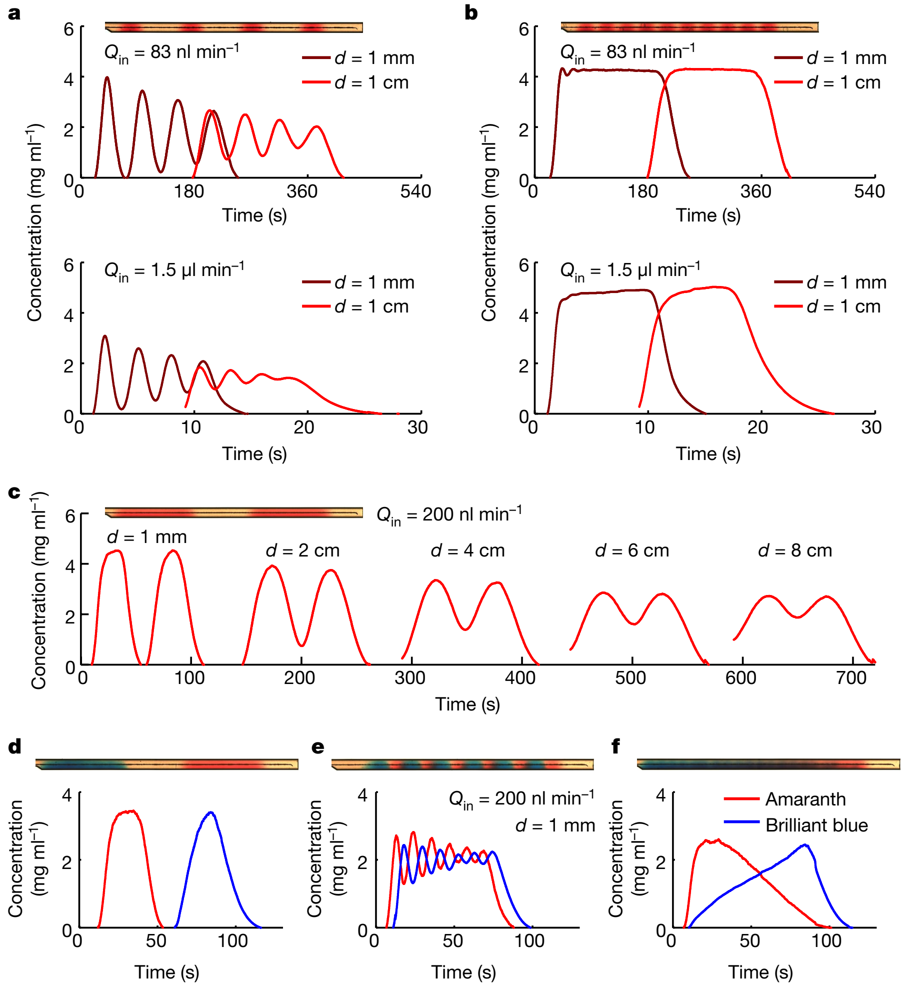

Fig. 4 | Reagent pulse shaping and generation of complex concentration profiles. These mean concentration profiles of reconstituted reagent were obtained using various deposition patterns, flow rates, Q_{in} values and measurement distances, d ($n = 6$ for each plot). The experimental profiles (optical micrographs) above the plots were obtained before the liquids exited the SCM (13-mm long). **a**, Well separated reagent spots disperse and acquire a broader concentration profile as they travel in the SCM and the downstream channel, at both the optimal flow rate, 83 nl min^{-1} (top) and a fast flow rate, 1.5 μl min^{-1} (bottom). **b**, Sufficiently dense spotting of reagents leads to homogenous concentration profiles. **c**, Evolution of the concentration domains of a reagent spotted at two main locations. **d**–**f**, Sequential delivery of two types of reagent, which were spotted such that they were well separated (**d**), co-homogenizing (**e**), or forming gradients (**f**).

G6PDH—a concentration 130 times lower than the 10% activity cut-off used in clinical tests to diagnose inherited G6PDH deficiency[24], which affects 400 million people worldwide[25].

Self-coalescence is a very general concept and applicable to other biochemical assays. We use it here also to perform isothermal recombinase polymerase amplification (RPA)[26] for the detection of DNA sequences of human papilloma virus (HPV) types 16 and 18 (Fig. 5d). For this implementation, the reaction master mix (containing enzymes, nucleotides, and so on) for RPA was deposited in SCM 1, and other reagents (primers, Mg^{2+} and SYBR Green dye) were deposited in SCM 2. The flow was paused for 3 min once SCM 1 was filled in order to allow complete reconstitution of the viscous RPA master mix. A self-timing SCM can also be used to delay the release of liquids (Extended Data Fig. 6 and Supplementary Information, section 2.3).

RPA is a more complicated chemical system than G6PDH quantification and requires finer optimization. For example, increasing the concentration of SYBR Green yields a better signal-to-noise ratio, but such intercalating dyes interfere with polymerase reactions and delay the onset of DNA amplification (Fig. 5e and Extended Data Fig. 7a). Similarly, amplification reactions accelerate with increasing Mg^{2+} concentration (Fig. 5f and Extended Data Fig. 7b), but too much Mg^{2+} can lead to unspecific amplification and high background noise owing to the formation of primer dimers. Reaction conditions can be readily mapped by spotting reagents in an SCM, as done here using step-function gradients of SYBR Green and Mg^{2+} (Fig. 5d). A DNA concentration gradient in an SCM can also be used to calibrate the real-time RPA reaction for quantifying DNA (Fig. 5g and Extended Data Fig. 7c). Moreover, different sets of primers can be deposited at different locations of SCMs for multiplexed detection of multiple target sequences (Fig. 5h, i) with high specificity and reproducibility (Fig. 5j).

The minimal dispersion of reagents in SCMs enables the localization of neighbouring reactions without compartmentalization, so that complex biochemical reactions can be implemented in nanolitre volumes of liquids in a single or several combined SCMs. This capability should have far-reaching consequences for biological assays and diagnostics, but could also prove to be a game-changing technology for chemistry at the microscale, and have impacts on the synthesis and discovery of new materials and research in the life sciences.

Online content

Any methods, additional references, Nature Research reporting summaries, source data, extended data, supplementary information, acknowledgements, peer review information; details of author contributions and competing interests; and statements of data and code availability are available at https://doi.org/10.1038/s41586-019-1635-z.

Received: 8 December 2018; Accepted: 21 August 2019;

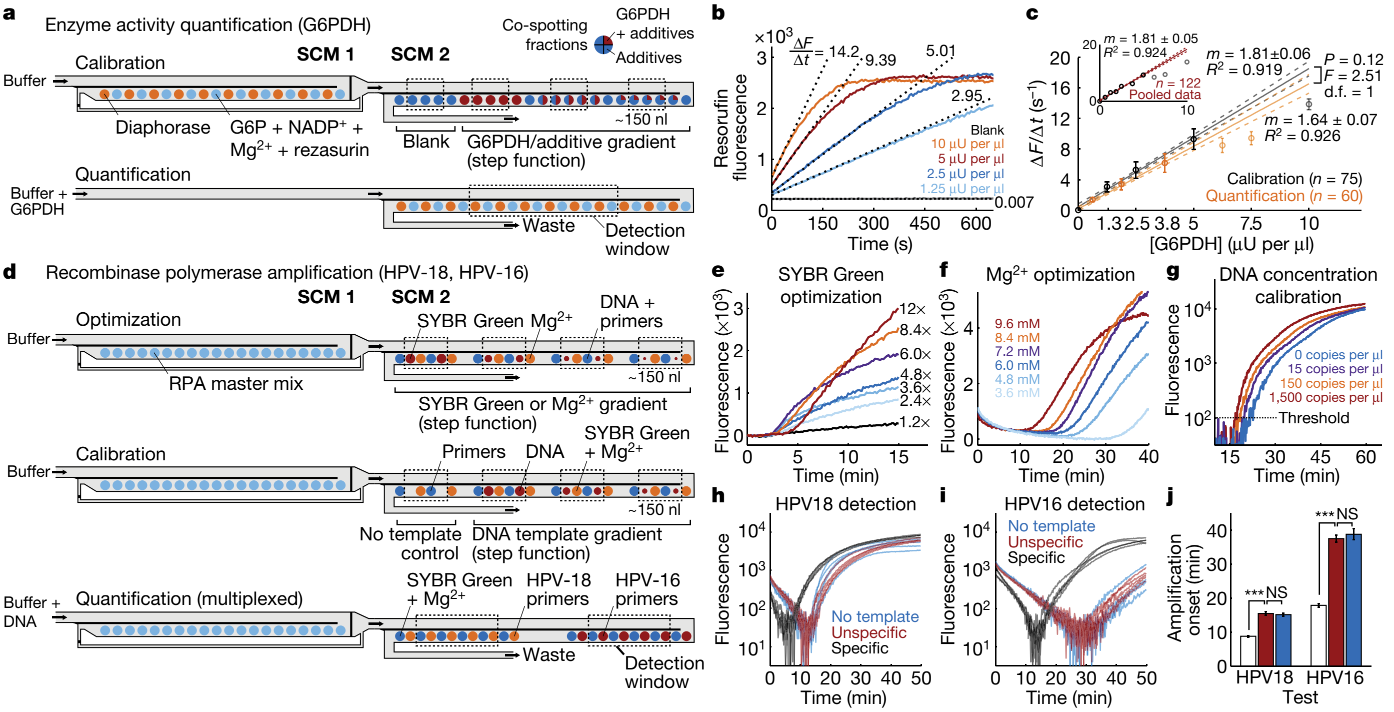

Fig. 5 | Biochemical reactions in SCMs. a, Implementation of a fluorometric reaction for quantifying active G6PDH. To calibrate the reaction (top), all reagents except the G6PDH analyte are deposited alternatingly into SCM 1, where they reconstitute and homogenize in a buffer before filling SCM 2. SCM 2 contains a G6PDH gradient and a counter gradient of additives. To quantify active G6PDH in a buffer (bottom), only one SCM is used. Fluorescence signals are measured over separate detection windows (dashed rectangles). Extra buffer from SCM 1 is purged at the entrance of SCM 2 using a vent/waste channel. **b**, Calibration data from a single experiment, based on the highest rate of change in resorufin fluorescence ($\Delta F/\Delta t$; dashed lines) at different G6PDH concentrations (coloured lines). **c**, Data from calibration (black) and quantification assays (orange) show a linear relationship between $\Delta F/\Delta t$ and G6PDH for low concentrations, and a saturation profile for higher concentrations (faint data points, omitted from the regression analysis), as expected for such an enzyme-concentration activity curve. The calibration and assay data are not significantly different (n, number of data points; m, slope of fit; d.f., degrees of freedom; error bars, standard deviation; calibration, ten experiments or more; quantification, five experiments or more). The inset shows the regression analysis of calibration and assay data pooled together. **d**, Implementation of RPA using SCMs, where SCM 1 contains the RPA reaction master mix and SCM 2 contains the rest of the reagents. RPA reaction kinetics are characterized locally by measuring fluorescence over concentration gradients of SYBR Green, Mg^{2+} or DNA template. A multiplexed quantification of DNA concentration can be realized by depositing primers for different templates in separate areas of SCM 2. **e**, **f**, Optimization data from single experiments at different SYBR Green (**e**) and Mg^{2+} (**f**) concentrations, for amplifying ten copies per microlitre of HPV-18 DNA. **g**, DNA concentration calibration data from one experiment for HPV-18 DNA quantification (threshold, 100). **h**, **i**, Individual traces (based on five experiments) of fluorescence signals from the HPV-18 detection window (**h**) and the HPV-16 detection window (**i**) when the test was run with no template (blue), with 1,000 copies per microlitre of unmatched template (unspecific, red), or with 1,000 copies per microlitre of matching template (specific, black). **j**, Amplification onset times from different tests (white, specific; red, unspecific; blue, no template). ***$P < 0.001$; NS, not significant; error bars, standard error of the mean.

1. Yager, P. et al. Microfluidic diagnostic technologies for global public health. *Nature* **442**, 412–418 (2006).
2. Hughes, T. R. et al. Expression profiling using microarrays fabricated by an ink-jet oligonucleotide synthesizer. *Nat. Biotechnol.* **19**, 342–347 (2001).
3. Derby, B. Printing and prototyping of tissues and scaffolds. *Science* **338**, 921–926 (2012).
4. Sirringhaus, H. et al. High-resolution inkjet printing of all-polymer transistor circuits. *Science* **290**, 2123–2126 (2000).
5. Gökçe, O., Mercandetti, C. & Delamarche, E. High-content optical codes for protecting rapid diagnostic tests from counterfeiting. *Anal. Chem.* **90**, 7383–7390 (2018).
6. Hitzbleck, M. & Delamarche, E. Reagents in microfluidics: an 'in' and 'out' challenge. *Chem. Soc. Rev.* **42**, 8494–8516 (2013).
7. Fridley, G. E., Le, H. Q., Fu, E. & Yager, P. Controlled release of dry reagents in porous media for tunable temporal and spatial distribution upon rehydration. *Lab Chip* **12**, 4321–4327 (2012).
8. Beck, M. et al. On-chip sample preparation by controlled release of antibodies for simple CD4 counting. *Lab Chip* **12**, 167–173 (2012).
9. Hitzbleck, M., Gervais, L. & Delamarche, E. Controlled release of reagents in capillary-driven microfluidics using reagent integrators. *Lab Chip* **11**, 2680–2685 (2011).
10. Garcia, E., Kirkham, J. R., Hatch, A. V., Hawkins, K. R. & Yager, P. Controlled microfluidic reconstitution of functional protein from an anhydrous storage depot. *Lab Chip* **4**, 78–82 (2004).
11. Hele-Shaw, H. S. The flow of water. *Nature* **58**, 34–36 (1898).
12. Oliver, J. F., Huh, C. & Mason, S. G. Resistance to spreading of liquids by sharp edges. *J. Colloid Interface Sci.* **59**, 568–581 (1977).
13. de Gennes, P. G., Brochard-Wyart, F. & Quéré, D. *Capillary Wetting Phenomena: Drops, Bubbles, Pearls, Waves* 225–226 (Springer, 2004).
14. Howison, S. Complex variable methods in Hele-Shaw moving boundary problems. *Eur. J. Appl. Math.* **3**, 209–224 (1992).
15. Goyette, P.-A. et al. Microfluidic multipoles theory and applications. *Nat. Commun.* **10**, 1781 (2019).
16. Driscoll, T. A. & Trefethen, L. N. *Schwarz–Christoffel Mapping* (Cambridge Univ. Press, 2002).
17. Bensimon, D., Kadanoff, L. P., Liang, S., Shraiman, B. I. & Tang, C. Viscous flow in two dimensions. *Rev. Mod. Phys.* **58**, 977–999 (1986).
18. Zimmermann, M., Schmid, H., Hunziker, P. & Delamarche, E. Capillary pumps for autonomous capillary systems. *Lab Chip* **7**, 119–125 (2007).
19. Vulto, P. et al. Phaseguides: a paradigm shift in microfluidic priming and emptying. *Lab Chip* **11**, 1596–1602 (2011).
20. Safavieh, R. & Juncker, D. Capillarics: pre-programmed, self-powered microfluidic circuits built from capillary elements. *Lab Chip* **13**, 4180–4189 (2013).
21. Zhao, B., Moore, J. S. & Beebe, D. J. Surface-directed liquid flow inside microchannels. *Science* **291**, 1023–1026 (2001).
22. Weiner, A. M. Femtosecond pulse shaping using spatial light modulators. *Rev. Sci. Instrum.* **71**, 1929–1960 (2000).
23. Guilbault, G. G. & Kramer, D. N. Fluorometric procedure for measuring the activity of dehydrogenases. *Anal. Chem.* **37**, 1219–1221 (1965).
24. LaRue, N. et al. Comparison of quantitative and qualitative tests for glucose-6-phosphate dehydrogenase deficiency. *Am. J. Trop. Med. Hyg.* **91**, 854–861 (2014).
25. Cappellini, M. & Fiorelli, G. Glucose-6-phosphate dehydrogenase deficiency. *Lancet* **371**, 64–74 (2008).
26. Piepenburg, O., Williams, C. H., Stemple, D. L. & Armes, N. A. DNA detection using recombination proteins. *PLoS Biol.* **4**, e204 (2006).

METHODS

Chip fabrication and reagent deposition. Silicon wafers with a 600-nm thermally grown oxide layer were processed using standard photolithography and deep reactive-ion etching (DRIE) (Extended Data Fig. 2a). Briefly, microchannels were patterned on the oxide layer using a 1.2-μm-thick AZ 6612 positive-tone photoresist and a glass/chromium photomask. Following a mild plasma cleaning to remove the photoresist residues and to activate the surface, the oxide layer was etched in buffered hydrofluoric acid (BHF). The photoresist was striped in a plasma asher and a new layer of AZ 6612 photoresist was spin-coated and patterned to define CPL geometries. The silicon substrate was anisotropically etched for 30 μm using DRIE (Alcatel AMS 200). Following the removal of the photoresist layer, both microchannels and CPLs were etched for 50 μm using DRIE and the oxide layer as a hard mask. Subsequently, the oxide layer was removed in BHF and the wafer was diced. The quality of the fabrication was verified using scanning electron microscopy (Zeiss Leo 1550) and optical interferometry (Veeco Wyco NT1100).

We also fabricated SCMs in a polymeric photoresist (SU-8) as part of capillary-driven microfluidic chips, and designed SCMs with relaxed dimensions and rounded corners for fabrication using injection moulding. SCMs should also be compatible with other replication techniques involving polydimethylsiloxane (PDMS) moulding and hot embossing.

We prefer using narrow trenches (5-μm wide) to create leading barriers and a step down to create diversion barriers (Extended Data Fig. 2b–f): this implementation has the advantage of not increasing the flow resistance over the CPL, is robust, and is easily fabricated in silicon channels of any thickness using standard lithography and DRIE (Extended Data Fig. 2a). Notwithstanding, protruding leading barriers (that is, a rail-like geometry) provide better stability than trenches for the same SCM height, because the smaller liquid–vapour interface leads to a proportionally larger Laplace pinning pressure. The geometry of the diversion barrier is not critical as this barrier is challenged only when the SCM is completely filled. However, if the gap between the leading barrier and the diversion barrier is too narrow (for example, less than 200 μm in 50-μm-deep SCMs), it pins the liquid, which in turn increases the pressure on the barriers and can result in their failure.

The surface of the microfluidic chips was cleaned using an air plasma (for 2 min with a coil power of 200 W; Tepla 100-E). Within 10 min after cleaning, the chips were silanized by immersing them in a solution of 0.1% trichloro(octyl)silane (Sigma-Aldrich) in heptane (Sigma-Aldrich) for 2 min. After rinsing the chips with ethanol (Fluka) and drying them under a stream of nitrogen, solutions of erioglaucine disodium (Sigma-Aldrich, hereon referred to as brilliant blue) and amaranth (Sigma-Aldrich), each at 30 mg ml^{-1} in water, were deposited in microfluidic structures using an inkjet spotter (Nano-Plotter 2.1, Gesim GmbH) equipped with a PicoTip-A piezoelectric pipette (Gesim GmbH). First, the reagents were spotted in two alignment marks (one visible in Extended Data Fig. 3) located at opposite sides of the chips. The difference between the programmed spotting coordinates and the effective location of spots was used to eliminate any misalignment. After spotting specific patterns of reagents on microfluidic chips, the chips were sealed with 3-mm-thick slabs of PDMS (Dow Corning Slygard 184). The volume of jetted droplets was measured by depositing 1,000 droplets of amaranth or brilliant blue solution at a spot on a clean surface, letting the spot dry, reconstituting the spot in 1 μl of water and measuring the concentration of the reconstitution with a spectrophotometer (Tecan Infinite M200). The volume of the droplets varied slightly from 40 pl to 60 pl between different spotting sessions, but was stable within the same session. The amount of deposited reagents was calibrated according to the droplet volume.

The patterns of reagents spotted in SCMs or control channels are detailed below. In experiments in which the dissolution in an SCM was compared with the dissolution in a control channel (Fig. 2d) and in volume scaling experiments (Fig. 3b), 5- to 15-mm-long lines comprising 25-ng spots (250-μm pitch) of amaranth were spotted. In experiments in which reagent pulse shaping was evaluated by using the amaranth dye (Fig. 4a–c), either four 100-ng spots (3-mm pitch; Fig. 4a), ten 100-ng spots (1-mm pitch; Fig. 4b) or two 3-mm-long lines comprising 25-ng spots (250-μm pitch) were spotted with 3-mm separation between the lines (Fig. 4c). In experiments in which the sequential delivery of multiple reagents was demonstrated (Fig. 4d), one 3-mm-long line comprising 15-ng spots (250-μm pitch) of amaranth and another one of brilliant blue were spotted with 3-mm separation between the lines. In experiments in which in situ mixing of multiple reagents was demonstrated (Fig. 4e), six 15-ng spots (1.5-mm pitch) of amaranth intercalated with six 15-ng spots (1.5-mm pitch) of brilliant blue were spotted. In experiments in which concentration gradients were generated (Fig. 4f), 30 spots (300-μm pitch) of amaranth gradually decreasing in mass from 15 ng to 0 ng were spotted over 30 spots (300-μm pitch) of brilliant blue gradually increasing in mass from 0 ng to 15 ng.

In the chips in which reagent pulse shaping was evaluated (Extended Data Fig. 8a), a narrow loop geometry[27] was used to minimize the effect of the turn on dispersion.

Particle image velocimetry. SCMs with a length of 15 mm, a width of 0.5 mm, a depth of 50 μm, and 5-μm-wide trenches were filled at a constant flow rate (active pumping, Kent Scientific Genie syringe pump, 0.5 μl min^{-1}) with a 10 μl min^{-1} fluorescein sodium (Fluka) aqueous solution containing 0.02% fluorescent microspheres (size 4.8 μm; Thermo-Scientific Fluoro-Max). The filling was imaged using a fluorescence microscope (Nikon Eclipse 90i, Nikon DS-1QM/H) at a rate of 15 frames per second (fps), with a 60-ms exposure per frame. The displacement of particles crossing the leading barrier during the 60-ms exposure was measured manually in each frame from the particle streaks on the images. These measurements were used to calculate the velocity of the particles. The position of the measured particles was determined from the midpoint of the streaks. In order to display the velocity streamlines as in Fig. 1b, 15 subsequent frames were aligned (taking the position of the curved meniscus as reference) in an image stack, the maximum projection of the image stack was taken, and the projected image was inverted. For this, images of the particles that sediment during longitudinal flow were manually removed from each frame for visual clarity. Fiji[28] was used for data extraction and image processing.

Optical measurements of reagent reconstitution. Microfluidic chips having SCMs or control microchannels spotted with reagents were placed under a stereo microscope (Leica MX16). The optical zoom, lighting intensity, and colour and exposure settings of the RGB CMOS camera (Leica MC170 HD) were identical for all experiments. Before the start of the experiments, the roll and the pitch of the microfluidic chips were corrected with a custom tiltable XY stage. A syringe pump (Kent Scientific Genie) was connected to the microfluidic chips with 1/32-inch tubing (Extended Data Fig. 9a). Before each experiment, the rate of pumping was calibrated. During the experiments, microfluidic chips were filled with water at a constant flow rate (indicated by Q_{in} for different sets of experiments). Videos (30 fps, 1,280 × 720 pixels) of the liquid carrying reconstituted reagents were recorded at fixed locations. Acquisition was stopped when the reagent solution was completely flushed away from the imaging area.

Video files were processed to extract the absorbance of solutions. This was done by defining a region of interest (ROI) on each video, centred on the downstream microchannel at a fixed distance (indicated by d for different sets of experiments) away from the diversion barrier. The ROIs were 200-μm wide and covered the width of the microchannel (180–500 μm). The mean intensity value over time of individual video channels was extracted from the area defined by the ROIs. For experiments with only amaranth dye, the intensity values from the green channel were used for further analysis; for experiments with amaranth and brilliant blue dyes, the intensity values from the red and blue channels were used. The absorbance signal was calculated by taking the negative logarithm of the quotient of the intensity values over the mean value of signal coming only from water.

The absorbance signal was converted into concentration values using calibration curves taken for different sets of experiments. For this, solutions of dyes with known concentrations were filled into the microfluidic chips and the intensity values were processed as described above. The exponential fit to the calibration data was used to transform the absorbance values to concentration values (Extended Data Fig. 1c, d). For experiments in which both amaranth and brilliant blue dyes were used, the calibration curves and the absorbance data were used after linear spectral unmixing[29] (Extended Data Fig. 8b–e). Matlab was used for these analyses.

General preparation for biochemical reactions in SCMs. To implement biochemical reactions using SCMs (Fig. 5), we fabricated microfluidic chips containing SCMs with protruding CPLs (that is, rails instead of trenches) in silicon and silanized them as above. These chips had a channel depth of 100 μm and 40-μm-high rails (Extended Data Fig. 2g, h). The reagents were deposited inside SCMs using the inkjet spotter equipped with a NanoTip piezoelectric pipette (GeSiM GmbH). The droplet volume for each reagent solution was characterized as above. After deposition of reagents, the chips were sealed using a PDMS that had been passivated by exposure to a 0.2% bovine serum albumin (BSA, Sigma-Aldrich) solution in 50 mM Tris-HCl (pH 7.5) for 10 min.

Spotting scheme for G6PDH reactions. To quantify G6PDH activity (Fig. 5a–c), we adapted a fluorometric protocol[23] for implementation inside SCMs.

All solutions were prepared in a 20 mM Tris-HCl (pH 7.8) buffer (Fluka) containing 0.2% BSA additive. Solutions containing diaphorase and G6PDH also contained 3% trehalose (Fluka) and 1 mM tris(2-carboxyethyl)phosphine (TCEP; Thermo Scientific).

In the calibration configuration, SCM 1 (width 0.5 mm, length 33 mm, rail width 30 μm; Extended Data Fig. 2g) was patterned using two solutions. The first solution contained 0.1 U μl^{-1} diaphorase (Sigma-Aldrich) and was deposited as discrete spots over a distance of 30 mm with a 1-mm pitch. Each spot was formed using four inkjet-deposited droplets (with a total volume of roughly 2.5 nl). The second solution contained the substrates and co-factors, namely 200 mM $MgCl_2$ (Sigma-Aldrich), 40 mM G6P (Sigma-Aldrich), 2 mM NADP$^+$ (Sigma-Aldrich) and 0.2 mM rezasurin (Sigma-Aldrich). The substrate solution was also deposited using a 1-mm pitch along 30 mm, but with a 0.5-mm shift relative to the diaphorase spots, and with each spot formed using eight dispensed droplets (approximately 4.5 nl).

SCM 2 (width 0.5 mm, length 30 mm) was patterned so as to have three regions with different G6PDH concentrations and one region without any G6PDH for blank measurements. Each region consisted of 5-mm-long lines of spots with a 0.5-mm pitch, and was separated from another region by 2 mm. In different experiment sets, either one (585 pl), two or four droplets of solution containing 0.52×10^{-4} U μl^{-1} G6PDH (Sigma-Aldrich), or two, four or eight droplets of the same solution, were deposited to form regions with increasing G6PDH concentration. In order to achieve comparable reaction kinetics from different regions, we needed to compensate for additives in the G6PDH solution that were also deposited at different amounts. This was achieved by spotting a solution containing only the additives over the spots of G6PDH to adjust the total deposited amount per spot to four or eight droplets.

In the quantification configuration, we used only SCM 2, and patterned it identically to SCM 1 in the calibration configuration.

Spotting scheme for recombinase polymerase amplification. We implemented isothermal recombinase polymerase DNA amplification[26] (RPA) using SCMs (Fig. 5d–j and Extended Data Fig. 7a–c) by adapting and applying the reagents from a commercially available kit (TwistDx TwistAmp Basic). Quantitative synthetic HPV-18 DNA (ATCC VR-3241SD) and quantitative synthetic HPV-16 DNA (ATCC VR-3240SD) were purchased and used in the amplification reactions as the template. Primer sequences were taken from the literature[30] and the primers were purchased (Integrated DNA Technologies). The following primers were used in the experiments (5′-3′):

HPV-16 forward: TTGTTGGGGTAACCAACTATTTGTTACTGTT
HPV-16 reverse: CCTCCCCATGTCTGAGGTACTCCTTAAAG
HPV-18 forward: GCATAATCAATTATTTGTTACTGTGGTAGATACCACT
HPV-18 reverse: GCTATACTGCTTAAATTTGGTAGCATCATATTGC

In all experiments, SCM 1 (width 1 mm, length 28 mm, rail width 75 μm, rail split with a 15-μm-wide trench; Extended Data Fig. 2h) was patterned with the 2× RPA master mix, prepared by reconstituting the pellet from the kit in 1 mM TCEP solution. The RPA master mix was deposited along a 25-mm line of spots, with a 1-mm pitch, and with each spot formed using 100 droplets (approximately 50 nl).

SCM 2 (width 0.5 mm, length 30 mm) was patterned with all other reagents necessary for the RPA reaction. For optimization of the SYBR Green concentration, a DNA-Mg mix consisting of 100 copies per microlitre of HPV-18 DNA, 140 mM magnesium acetate (MgOAc; Fluka), 5 μM of each HPV-18 primer, 3% trehalose and 0.2% BSA was deposited as a 28-mm line of spots with a 0.5-mm pitch, and with each spot formed using five droplets (approximately 3 nl). Over these spots, a step-function-like gradient of SYBR Green was created by depositing a 50× SYBR Green (Invitrogen) solution containing 0.2% BSA along 4-mm segments having a 0.5-mm pitch, with the segments formed either with one (roughly 600 pl), two, three, four, five, seven or ten droplets, without additional spacing between segments.

For optimization of the Mg^{2+} concentration, a 24-mm line of spots of DNA solution, containing 250 copies per microlitre of HPV-18 DNA, 12.5 μM of each HPV-18 primer and 3% trehalose, was patterned in SCM 2 with a 0.5-mm-pitch and with each spot formed by two droplets (approximately 1.2 nl). A similar second line, which was formed using spots (two droplets, approximately 1.2 nl) of 125× SYBR Green, 75 mM MgOAc, 3% trehalose and 0.2% BSA, was patterned with a 0.25-mm shift from the first line. Over the second line, a step-function-like gradient of Mg^{2+} was formed by depositing 50 mM MgOAc solution on 4-mm segments having a 0.5-mm pitch, and with the segments formed either by zero, one (roughly 600 pl), two, three, four or five droplets, and no additional spacing between segments.

For calibration of DNA concentration to amplification onset time, two 18-mm lines each with a 0.5-mm pitch and spots of two droplets (roughly 1.2 nl) were patterned with a 0.25-mm offset between them. The first line consisted of spots of 125× SYBR Green, 95 mM MgOAc, 3% trehalose and 0.2% BSA. The second line consisted of spots of 95 mM MgOAc, 8.4 μM of each HPV-18 primer and 3% trehalose. Over the second line, a step-function-like gradient of HPV-18 DNA was patterned by depositing two droplets (roughly 1.2 nl) of DNA solution containing 3% trehalose along 4-mm segments with a 0.5-mm pitch, with the segments spotted from different DNA solutions having 250, 2,500 or 25,000 copies per microlitre of HPV-18 DNA. No calibration was performed for HPV-16.

For multiplexed detection of HPV-16 and HPV-18 DNA, SCM 2 was patterned similarly to the spotting scheme for DNA calibration, but without any DNA spotted. Additionally, one half of SCM 2 was patterned using HPV-16 primers and the other half using HPV-18 primers.

Biochemical reactions in SCMs, data acquisition and analysis. To start the biochemical reactions, spotted and sealed chips were filled only with buffer, or with buffer containing G6PDH or DNA under active pumping at varied flow rates and at room temperature (Extended Data Fig. 9a). Each chip carried elements for five experiments. Experiments were run one after another. In all experiments, SCM 1 was filled at a rate of 1.0 μl min^{-1}, and SCM 2 at 0.5 μl min^{-1} during longitudinal flow and 3.5 μl min^{-1} during self-coalescing flow. For RPA reactions, the flow was paused for 3 min after SCM 1 was filled for the rehydration and reconstitution of the RPA master mix.

For calibration of the G6PDH reaction, the chips were filled with 50 mM Tris-HCl (pH 7.8) solution. For G6PDH quantification experiments, chips were manually filled using a micropipette (Extended Data Fig. 9b) with 50 mM Tris-HCl (pH 7.8) solutions containing 0.625–7.5 μU μl^{-1} G6PDH, 0.2 mM TCEP, 0.6% trehalose and 0.04% BSA.

For calibration of the RPA reaction and for optimization of SYBR Green and MgOAc concentrations, the chips were filled with 25 mM Tris-HCl (pH 7.9) solution containing 100 mM potassium acetate (Sigma-Aldrich), 5.4% polyethylene glycol (molecular weight 35 kDa; Sigma-Aldrich) and 0.05% Tween-20 (Fluka). For the multiplexed detection of HPV-16 and HPV-18, the chips were filled with the same solution additionally containing 1,000 copies per microlitre of HPV-16 or HPV-18 DNA.

After the chips were filled, they were swiftly transferred to a microtitre plate reader (Tecan Infinite M200) using a custom-made aluminium adaptor (Extended Data Fig. 9c). While the reactions ran, the reader scanned along SCM 2 and measured the fluorescence signal every millimetre. G6PDH reactions were run at 25 °C. The conversion of rezasurin to resorufin was measured at 560-nm excitation and 595-nm emission using a sampling time interval of 5 s. RPA reactions were run at 33–36 °C. SYBR Green fluorescence was measured using 490-nm excitation and 525-nm emission wavelengths every 10 s. Subsequent analyses were run only on the measurements taken at detection windows (roughly 150 nl, determined by the point spread function of the excitation beam of the plate reader; full width at half maximum roughly 3 mm as measured), centred over regions with different concentrations of G6PDH, SYBR Green, Mg^{2+} or DNA (for optimization and calibration), or at detection windows centred over regions with G6PDH assay reagents or primers (for quantification).

The kinetics of the G6PDH reaction was characterized from the fastest rate of fluorescence change ($\Delta F/\Delta t$) for each reaction at different G6PDH concentrations[31]. The quality of the calibration curve was assessed using linear regression (LinearModel class in Matlab). To evaluate whether calibration and quantification experiments agreed, we applied analysis of covariance (ANCOVA; 'aoctool' function in Matlab).

The amplification onset of RPA reactions was extracted first by subtracting the background from the signal and later by applying a threshold to the logarithm of the data. The quality of the calibration curve was assessed using linear regression (LinearModel class in Matlab). To test whether detection of HPV-16 or HPV-18 DNA produced signals with significantly earlier onset times than unspecific amplification, we applied a two-sample *t*-test ('ttest2' function in Matlab).

Finite element method for characterization of self-coalescing flow. The finite-element method (FEM) platform COMSOL Multiphysics was used to model the SCM and simulate 3D laminar and 2D potential flows. Both geometries were defined using COMSOL's CAD tools. The parameters used in the models are shown in Extended Data Table 1. The 3D laminar and 2D potential flows were respectively defined using COMSOL's 'laminar flow' and 'mathematics' modules—that is, incompressible Navier–Stokes equation and Laplace equation. In both cases, the problem is solved in the reference frame of the moving meniscus (the $Z*$ domain in Supplementary Information section 1) and plotted in the laboratory reference frame (the Z domain) with the transformation $z* = z + Ut$. This equivalence specifically implies the invariance property of the Navier–Stokes equation under a Galilean transformation. These equations were both solved using the built-in steady-state fully coupled solver. Elements were manually refined on the boundary of the meniscus to obtain sufficient numerical accuracy. Parametric sweeps were used to study the impact of the total width, contact angle and flow rate on the velocity field. The orthogonal velocity component was taken from a line going through the SCM along the x axis at different y positions and at mid-height in the Navier–Stokes case.

Data availability

The data that support the findings of this study are available from the corresponding authors on request.

Code availability

The code for the Schwarz–Christoffel mapping of self-coalescence (using Matlab), as well as the code for reagent pulse shaping (using Maple), is available on request from T.G.

27. Paegel, B. M., Hutt, L. D., Simpson, P. C. & Mathies, R. A. Turn geometry for minimizing band broadening in microfabricated capillary electrophoresis channels. *Anal. Chem.* **72**, 3030–3037 (2000).

28. Schindelin, J. et al. Fiji: an open-source platform for biological-image analysis. *Nat. Methods* **9**, 676–682 (2012).
29. Zimmermann, T. Spectral imaging and linear unmixing in light microscopy. *Adv. Biochem. Eng. Biotechnol.* **95**, 245–265 (2005).
30. Seaman, W. T. et al. Detection and quantitation of HPV in genital and oral tissues and fluids by real time PCR. *Virol. J.* **7**, 194 (2010).
31. Glock, G. E. & McLean, P. Further studies on the properties and assay of glucose 6-phosphate dehydrogenase and 6-phosphogluconate dehydrogenase of rat liver. *Biochem. J.* **55**, 400–408 (1953).

Acknowledgements O.G., Y.T. and E.D. thank W. Riess for continuous support, and acknowledge partial funding from the European Union's 7th Framework programme Chips4Life project (278720) and the IBM Research Frontiers Institute. O.G. and E.D. thank Coris BioConcept for discussions on DNA-amplification technologies, and microfluidic ChipShop for the fabrication of polymer prototypes using injection moulding. T.G. thanks C. Boudoux and S. Prudhomme (from the École Polytechnique de Montréal) for useful discussions. T.G. acknowledges support from the Natural Sciences and Engineering Council of Canada (NSERC; RGPIN2014-06409), the Fonds de Recherche du Québec–Nature et Technologies (FRQNT), and CMC microsystems.

Author contributions E.D. conceived the research. O.G. discovered self-coalescing flows, designed SCMs and experiments, and conducted the experiments. T.G. developed the theoretical framework and contributed to the experimental design. S.C. performed the conformal mapping calculations and the numerical simulations, and contributed to the theoretical framework. O.G., S.C. and T.G. analysed the data. Y.T. fabricated microfluidic chips and documented them using scanning electron microscopy. O.G., T.G. and E.D. wrote the manuscript. All authors discussed and provided input to the manuscript.

Competing interests The authors declare no competing interests.

Additional information

Supplementary information is available for this paper at https://doi.org/10.1038/s41586-019-1635-z.

Correspondence and requests for materials should be addressed to T.G. or E.D.

Peer review information *Nature* thanks Piotr Garstecki and the other, anonymous, reviewer(s) for their contribution to the peer review of this work.

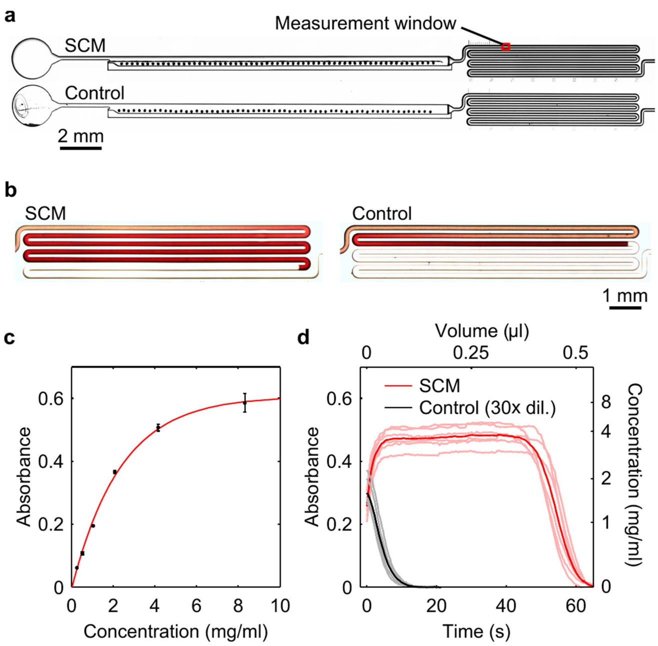

Extended Data Fig. 1 | Characterization of reagent dissolution in SCMs and control experiments. a, Bright-field microscope images of microfluidic chips in silicon, each chip being composed of a rounded inlet (left), an SCM (middle), and a meandering channel (right) used for conveniently measuring the concentration profile of the solution exiting the SCM. **b**, Amaranth solutions from an SCM (left) and in a control microchannel (right) are readily visualized using the meandering channels. **c**, Calibration curve for quantification of the concentration of reconstituted amaranth ($n = 4$ for each concentration). Error bars represent standard error of the mean. **d**, Concentration profiles of amaranth solution reconstituted in SCMs or control microchannels ($Q_{\mathrm{in}} = 500$ nl min^{-1}). Means of individual acquisitions are displayed with dark coloured lines and individual acquisitions with a lighter shading. Amaranth solution was inkjet spotted into SCMs at 100 ng mm^{-1} (250-μm pitch). The reagent accumulation in the control was so strong that the amaranth solution was diluted ×30 before deposition to keep the absorbance signal in the dynamic range of the camera. The concentration profile from control experiments shown in Fig. 2d is scaled up from this diluted signal.

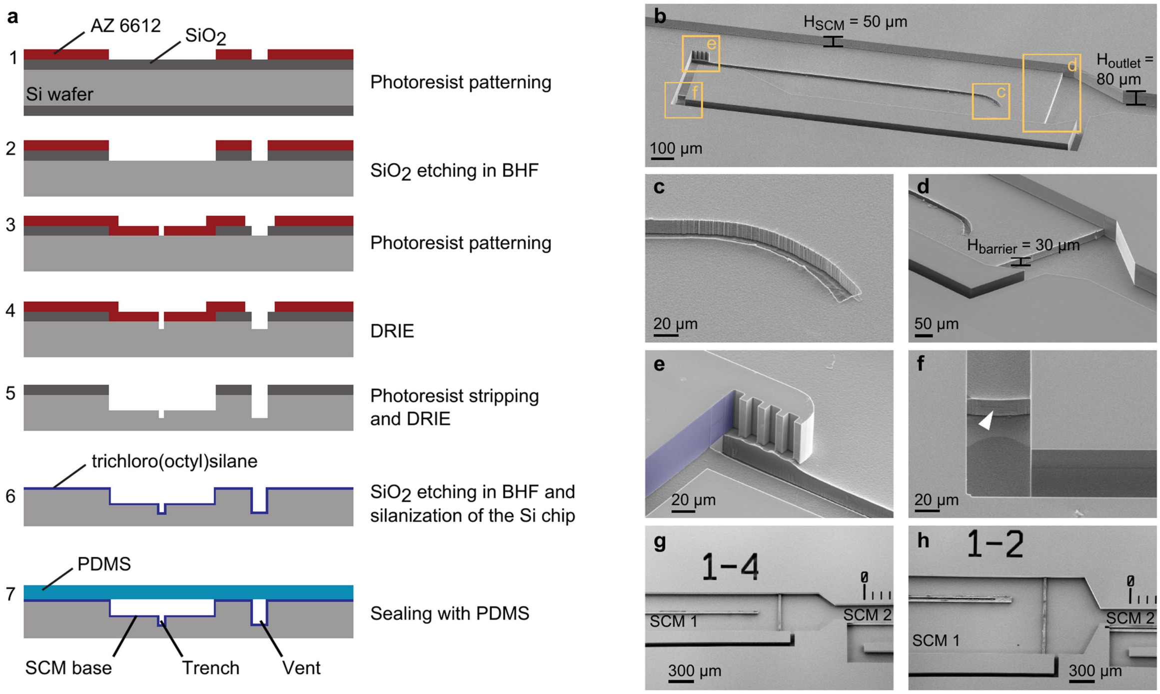

Extended Data Fig. 2 | Fabrication steps for SCMs with depressed barriers, and scanning electron microscopy images of representative SCMs. **a**, Silicon wafers are processed by standard photolithography and multiple steps of deep reactive-ion etching (DRIE). Specifically, a 1.2-μm-thick AZ 6612 photoresist layer is patterned (step 1) to mask the SiO$_2$ layer during etching in buffered hydrofluoric acid (BHF; step 2). A new layer of AZ 6621 is patterned (step 3), exposing the areas that are etched to form the trenches during the first DRIE step (step 4). Later, using the patterned SiO$_2$ layer as the mask, a second DRIE step forms the microchannels while preserving the trenches (step 5). After dicing, the chips are cleaned and silanized in trichloro(octyl)silane solution (step 6). After reagent deposition, chips are sealed with a layer of polydimethylsiloxane (PDMS; step 7). **b**, Image of an SCM fabricated in silicon, with yellow frames highlighting particular regions shown below. **c**, The leading barrier with a trench geometry. Here, for visual clarity, the trench width is 20 μm, but 5-μm-wide trenches were used in experiments. The curved end of the leading barrier facilitates the initiation of self-coalescing flow. **d**, Diversion barrier with a step-down geometry. **e**, Raised vertical CPLs at the entrance of the SCM help to keep the meniscus away from the side wall coloured in blue. **f**, The barrier at the vent entrance (arrowhead) ensures that liquid does not enter the vent. The depths of the SCM (H_{SCM}), outlet (H_{outlet}) and barriers (H_{barrier}) are shown on the images. **g**, **h**, Scanning electron microscopy (SEM) images of the devices used in G6PDH reactions (**g**) and in RPA reactions (**h**). (The numbers 1-2 and 1-4 are device numbers.).

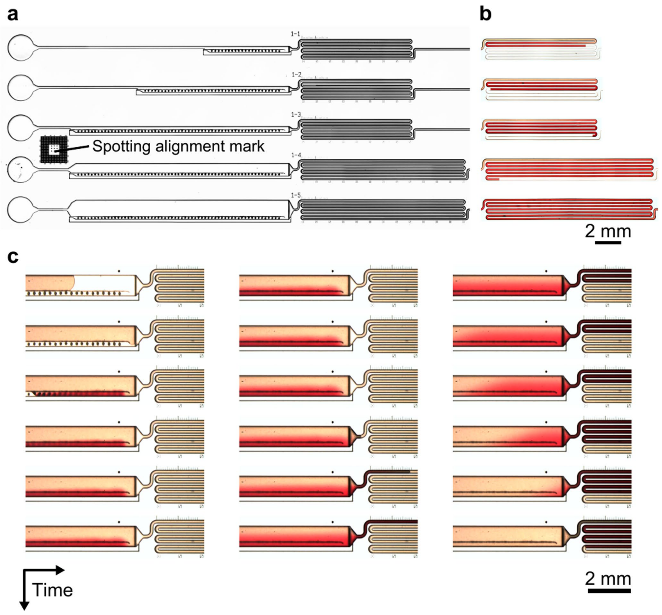

Extended Data Fig. 3 | SCM volume scaling experiments. a, Bright-field microscope images of devices fabricated in silicon (numbered 1-1 to 1-5) in which volume scaling experiments were performed. As discussed in Fig. 1d, the velocity of the self-coalescing flow decays more quickly in narrower than in wider SCMs. In order to maintain a quick decay of the self-coalescing flow velocity in wide SCMs, the leading barrier is simply shifted towards the area in which reagents are deposited. Amaranth is deposited at 100 ng mm^{-1} (250-μm pitch). A spotting alignment mark is used to align the inkjet spotter head with the microfluidic chips for precise targeting of the deposition location. **b**, Bright-field microscope images showing the amaranth solution in the meandering channels, reconstituted in the SCMs shown in panel **a**. **c**, Time series of bright-field microscope images showing the reconstitution of amaranth in a 1-mm-wide SCM ($Q_{\mathrm{in}} = 500$ nl min^{-1}). Typically, in wide SCMs (wider than 0.5 mm), lateral homogenization of the reconstituted reagent is complete at the narrow outlet of the SCM (as seen here), and can be enhanced, if necessary, by adding a Dean vortex mixer, a chaotic mixer, or a simple meandering channel. Larger volumes of solution with reconstituted reagents can also be achieved using an array of parallel SCMs. SCMs are easily scaled; however, making them longer decreases the maximum filling flow rate because the pressure at the inlet needs to be lower than the Laplace pressure over the CPL.

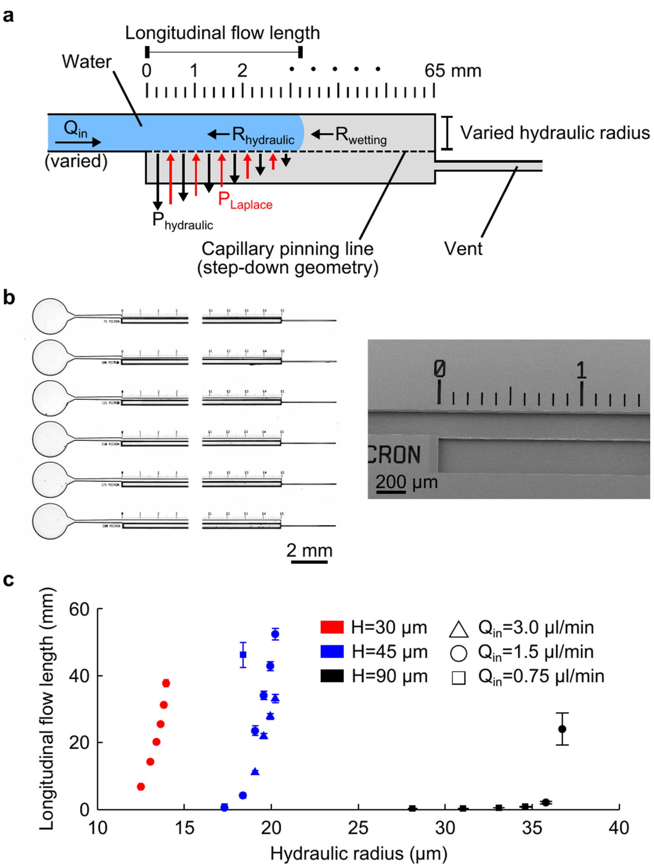

Extended Data Fig. 4 | Assessment of the stability of the leading barrier. **a**, During longitudinal flow, the hydraulic pressure ($P_{\mathrm{hydraulic}}$) increases as the hydraulic resistance ($R_{\mathrm{hydraulic}}$) increases with the distance travelled by the liquid. The leading barrier is able to preserve the longitudinal flow as long as the pinning forces (P_{Laplace}) can balance the increasing hydraulic pressure and the pressure exerted by the resistance to wetting (R_{wetting}). In order to investigate this effect, the width ($W = 75$, 100, 125, 150, 175 or 200 µm) and the height ($H = 30$, 45 or 90 µm) of the longitudinal flow area and the filling flow rate ($Q_{\mathrm{in}} = 0.75$, 1.5 or 3.0 µl min^{-1}) were varied. During experiments, the maximum distance along which the liquid remains pinned was measured. **b**, Bright-field (left) and SEM (right) images of devices in which stability-assessment experiments are performed. **c**, Experimental data support theoretical predictions that: first, a smaller liquid–vapour interface can bear a higher hydraulic pressure; second, the hydraulic radius of the longitudinal flow area needs to be large in order to fill deeper structures or for high filling flow rates; and third, the flow rate challenges the stability of the leading barrier. Data points are means of experiments ($n = 8$ or more; error bars represent standard error of the mean). Conditions in which the liquid was not pinned at the CPL (longitudinal flow length = 0 mm) or the liquid travelled to the end of the test device (longitudinal flow length = 65 mm) are excluded from the plot.

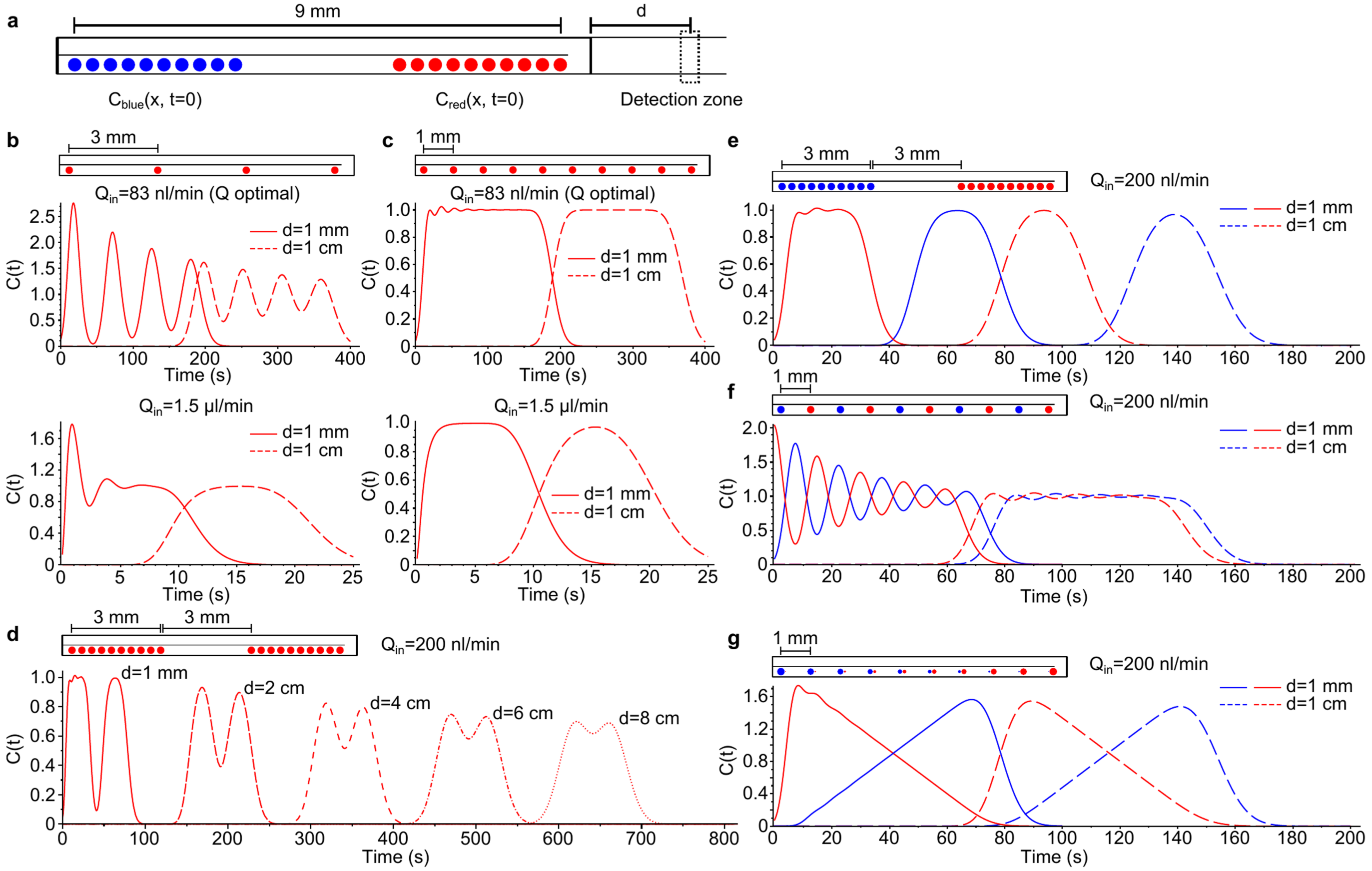

Extended Data Fig. 5 | Predicted complex concentration profiles from diffusion–dispersion models. a, Illustration of the experimental method for analysing dispersion in SCMs and in downstream channels at distance *d*. C, concentration. **b**–**g**, Predicted concentration profiles for experiments shown in Fig. 4 ($C(t)$ in arbitrary units). **b**, **c**, Results of controlling the spotting pitch to generate spiked (**b**) or flat (**c**) concentration pulses at optimal (Pé = 5.6; top panels) and large (Pé = 100; lower panels) Péclet numbers, at constant spotted reagent mass. **d**, Signal decorrelation over time due to Taylor–Aris dispersion for several positions of the detection zone (Pé = 13). **e**, Pulsing of two spatially resolved different reagents (Pé = 13). **f**, Pulsing of a flat profile of two mixed reagents by alternated spotting and flow control (Pé = 13). **g**, Pulsing of two linear concentration gradients to a detection zone (Pé = 13).

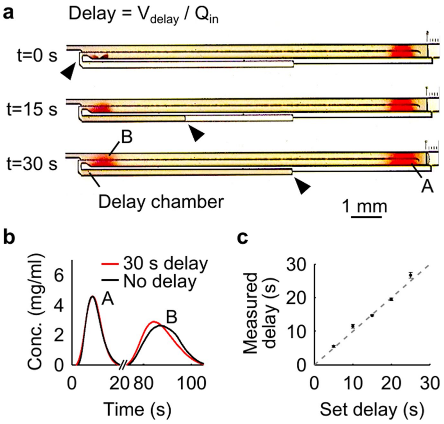

Extended Data Fig. 6 | Release of reconstituted reagents from an SCM with time delays. A chamber of volume V_{delay} at the entrance of the vent adds a delay before a liquid leaves the SCM. **a**, Time series of images showing filling of the delay chamber while reconstituted amaranth diffuses. Reagents in area A, but not in area B, have additional time to reconstitute/diffuse while the rest of the SCM fills ($t = 0$ s). If needed, using a delay chamber gives additional time for the reconstitution/diffusion of the B reagents. Arrowheads mark the liquid filling front in the delay chamber. **b**, Effect of delay on the concentration profile of points A and B. Without any delay, point B disperses more than it does with a delay, and its profile is broader ($n = 9$; $Q_{\text{in}} = 200$ nl min^{-1}). **c**, Measured delay provided by different delay chambers. The dashed line is the identity line; error bars represent standard error of the mean; $n = 6$; $Q_{\text{in}} = 200$ nl min^{-1}.

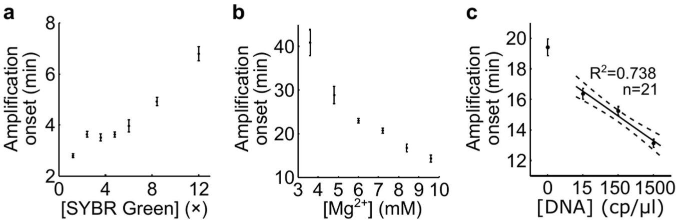

Extended Data Fig. 7 | Optimization and calibration of RPA reactions in SCMs. a, **b**, Optimization data for SYBR Green concentration (**a**; four experiments) and Mg^{2+} concentration (**b**; five experiments) for amplification of ten copies per microlitre of HPV-18 DNA. **c**, DNA concentration calibration (seven experiments) for HPV-18 DNA quantification. Plots show amplification onset time extracted from SYBR Green fluorescence signals. Error bars represent standard errors of the mean.

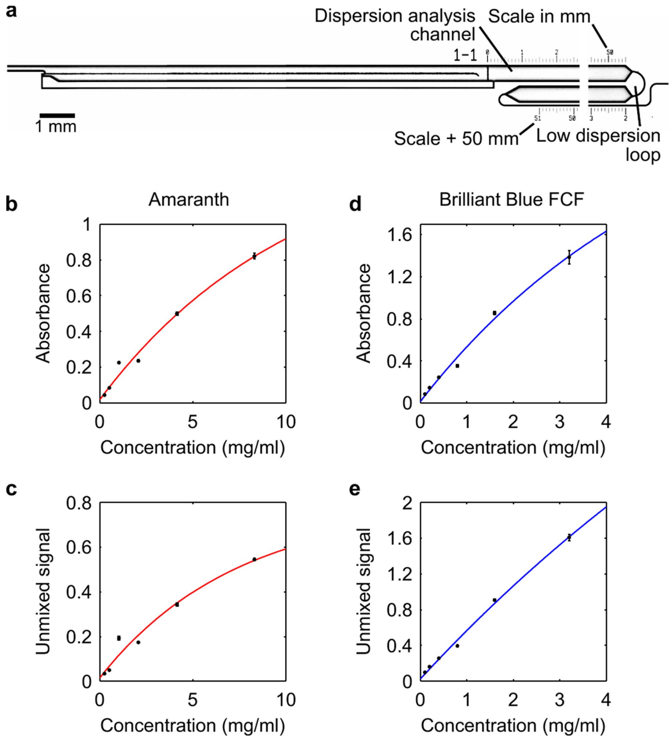

Extended Data Fig. 8 | Characterization of dissolution of multiple reagents in SCMs. a, Bright-field image of the device in which reagent pulse shaping and complex profile generation experiments were performed. The diversion barrier of these SCMs has a trench geometry in order to keep the dimensions of the dispersion analysis channel identical to the dimensions of the SCM. **b**, Absorbance calibration curve, and, **c**, the calibration curve after linear spectral unmixing of the amaranth signal. **d**, **e**, As for panels **b**, **c**, but for the brilliant blue signal. $n = 6$ for each data point. Error bars represent standard errors of the mean.

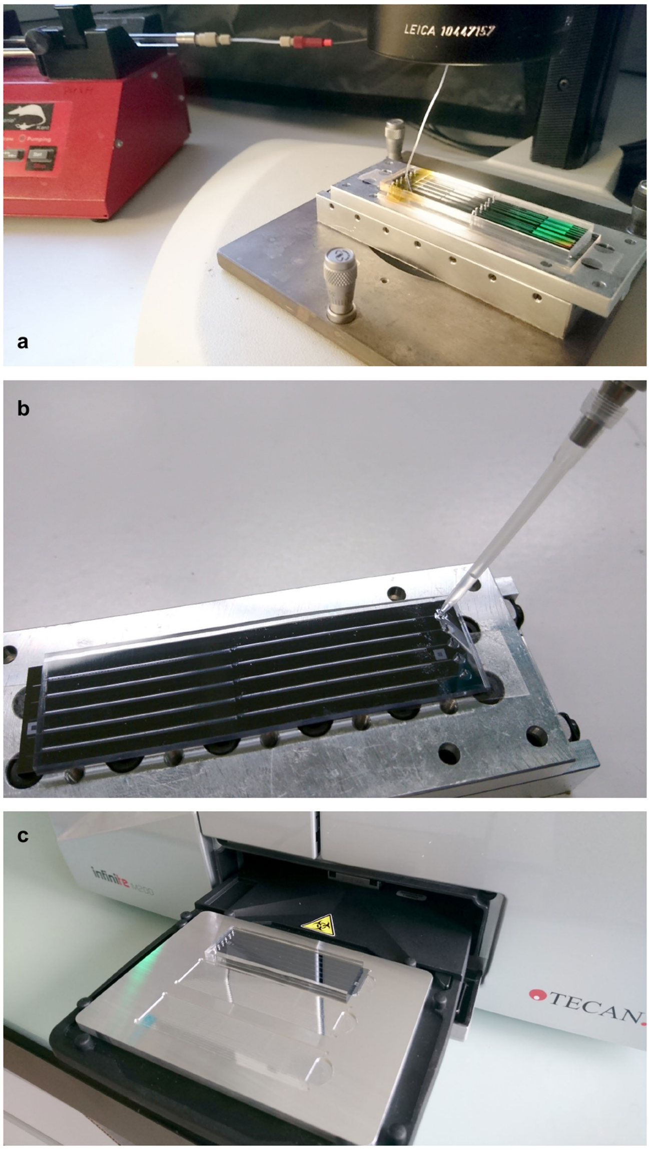

Extended Data Fig. 9 | Experimental setup. a, The setup for filling SCMs and documenting the dissolution of food dyes. **b**, Filling SCMs manually using a micropipette for G6PDH quantification experiments. **c**, Measuring the fluorescence signal from G6PDH and RPA reactions using a microtitre plate reader fitted with a custom-made aluminium adaptor.

Extended Data Table 1 | The parameters used in simulations

Variable	Description	Value
H	Channel height	50 µm
W	Channel total width	500 µm
L	Channel length	1 cm
θ_w	Contact angle (experimentally measured)	varies (default: 116°)
Q	Flow rate	0.5-1.5 µl/min
ρ_{H_2O}	Water density at ~20°C	1 kg/m^3
η_{H_2O}	Water dynamic viscosity at ~20°C	1 mPa·s